

DOI: 10.1002/adfm.200500841

# Sacrificial-Layer Atomic Layer Deposition for Fabrication of Non-Close-Packed Inverse-Opal Photonic Crystals\*\*

By Elton Graugnard, Jeffrey S. King, Davy P. Gaillot, and Christopher J. Summers\*

A method is presented for predicting and precisely controlling the structure of photonic crystals fabricated using sacrificial-layer atomic layer deposition. This technique provides a reliable method for fabrication of high-quality non-close-packed inverse shell opals with large static tunability and precise structural control. By using a sacrificial layer during opal infiltration, the inverse-opal pore size can be increased with sub-nanometer resolution and without distorting the lattice to allow for a high degree of dielectric backfilling and increased optical tunability. For a 10 % sacrificial layer, static tunability of 80 % is predicted for the inverse opal. To illustrate this technique, SiO<sub>2</sub> opal templates were infiltrated using atomic layer deposition of ZnS, Al<sub>2</sub>O<sub>3</sub>, and TiO<sub>2</sub>. Experimentally, a static tunability of over 600 nm, or 58 %, was achieved and is well described by both a geometrical model and a numerical-simulation algorithm. When extended to materials of higher refractive index, this method will allow the facile fabrication of 3D photonic crystals with optimized photonic bandgaps.

## 1. Introduction

Photonic crystals have been studied extensively for their potential to control and manipulate light,<sup>[1,2]</sup> similar to the way electrons are controlled in a semiconductor,<sup>[3]</sup> opening the door to high-speed, low-power, all-optical devices. A common method for fabricating 3D photonic crystals is the infiltration and subsequent inversion of synthetic opal templates to create inverse opals consisting of air spheres in a face-centered-cubic (fcc) dielectric backbone.<sup>[4–7]</sup> For a sufficiently high dielectric/air refractive-index contrast ( $n > 2.8$ ), the inverse opal is predicted to possess a complete photonic bandgap (PBG),<sup>[8]</sup> which has been demonstrated for Si and Sb<sub>2</sub>S<sub>3</sub> inverse opals for which  $n > 3.3$ .<sup>[9–11]</sup> To improve the quality and control of inverse-opal fabrication, several groups have developed surface-limited growth techniques, such as atomic layer deposition (ALD) and certain chemical vapor deposition (CVD) processes.<sup>[7,12–16]</sup> Recently, several groups have reported strategies to increase the width of the complete PBG in inverse opals by controlling the dielectric infiltration and/or modifying the underlying opal template.<sup>[8,17,18]</sup> For example, leaving small air pockets at the centers of the opal void spaces by controlling the filling fraction,  $f$ , of the infiltrated dielectric produces inverse shell opals

and was predicted to increase the width of the PBG ( $\Delta\omega/\omega$ ) relative to a fully infiltrated inverse opal ( $f = 0.26$ ).<sup>[8]</sup> In a second method, Doosje et al. predicted that the PBG width can be increased by modifying the inverse opal unit cell such that the radius of the air spheres,  $R$ , is decreased relative to the original opal-sphere radius ( $R < R_{\text{opal}}$ ) to form a non-close-packed (NCP) inverse opal.<sup>[17]</sup> Based on this NCP geometry, a gap between the eighth and ninth photonic bands of almost 10 % is predicted for an optimized silicon ( $n = 3.45$ ) NCP inverse opal. Thus, control over the construction and shape of the high-dielectric regions in the fcc lattice can be used to significantly affect the optical properties of a 3D photonic crystal.

Experimentally, NCP inverse opals can be fabricated by backfilling or conformally adding additional dielectric material into the cavities of the inverse opal. This reduces the air-sphere radius to less than the original opal-sphere radius ( $R < R_{\text{opal}}$ ), thereby creating an NCP structure. While the NCP structure is predicted to have an enhanced complete PBG for high-dielectric backbones such as Si, for lower-dielectric backbone materials the Bragg peak and high-order flat bands are likewise strongly affected by the NCP structure. For inverse opals formed from low-index backbone materials, conformal backfilling provides a mechanism to statically tune the optical properties such as the width and position of the Bragg peak. However, for both high- and low-index structures, backfilling is severely limited by the small pores in conventional inverse opals, which seal too quickly to create an NCP structure and prevent a large degree of tunability. Recently, Míguez et al. and King et al. reported techniques to partially overcome this limitation by using extended heavy presintering of the opal template to increase the necking (or overlap) between neighboring spheres, thus increasing the inverse-pore diameter and allowing a higher degree of backfilling.<sup>[18,19]</sup> Although this technique can lead to enhanced properties, heavy presintering is

[\*] Prof. C. J. Summers, Dr. E. Graugnard, Dr. J. S. King, D. P. Gaillot  
School of Materials Science and Engineering  
Georgia Institute of Technology  
771 Ferst Drive NW, Atlanta, GA 30332-0245 (USA)  
E-mail: chris.summers@mse.gatech.edu

[\*\*] This work was supported by the U.S. Army Research Office under MURI contract DAAD19-01-1-0603. We also thank S. Blomquist and the U.S. Army Research Lab for assistance with the ZnS ALD.

unable to provide the nanometer-scale precision and control required to produce high-quality inverse opals. Additionally, it is incompatible with many template materials and structures. Thus, to overcome these limitations and fabricate optimized and tunable inverse-opal-based photonic crystals, a new technique is needed to meet the challenges of depositing low-porosity, high-index, dielectric materials within the complex, sharp, 3D nanoscopic features found in opal and inverse-opal templates.

Here, we present a new concept that overcomes the limitations of conventional or presintered inverse opals and allows precisely controlled fabrication of NCP inverse-shell opals. In this paper we demonstrate, using sacrificial-layer ALD in opal templates, the fabrication and tuning of high-quality NCP  $\text{TiO}_2$  inverse-shell opals with unprecedented control over the nanoscale structure and dielectric filling fraction, from an ultralow 5% to over 60%. The precise control enables tuning of the Bragg diffraction peak over 600 nm (greater than the visible spectral region and larger than has ever been reported for an inverse opal), while simultaneously enhancing the width of the optical stop band by 67%, with no increase in structural disorder. Although incapable of opening a full PBG in an inverse opal, in the current study we have used  $\text{TiO}_2$  in order to both realize photonic crystals for use in the spectral region from visible to near-IR wavelengths (vis-NIR), and to demonstrate nanostructured  $\text{TiO}_2$  devices for applications in photovoltaics, photocatalysis, gas sensing, and biocompatible materials, where  $\text{TiO}_2$  has many desirable properties. Compared with other deposition techniques, the sub-nanometer digital control of sacrificial-layer ALD allows uniform and precisely measured growth in nanoscale templates without producing undesired growth by-product formations. Furthermore, the availability of low-temperature ALD (less than 80 °C for  $\text{Al}_2\text{O}_3$  and  $\text{TiO}_2$ ) allows application to polymer and bioderived templates that would not survive the temperatures (> 800 °C) required for sintering. Lastly, one of the key features of this technique is the ability to statically tune as-fabricated structures over a very large range which, in the current study, was achieved by conformally backfilling the inverse opal with controlled depositions of additional  $\text{TiO}_2$  to an ultimate filling fraction of 62%.

### 1.1. Sacrificial-Layer ALD Model

The fabrication protocol for creating an NCP inverse opal using the multilayer ALD technique can be divided into three main stages: 1) infiltration of a template with both a sacrificial buffer layer and the desired dielectric material; 2) inversion of the structure by removing both the original template and the sacrificial layer; and 3) re-infiltration, or backfilling, of the new template with additional dielectric material. These stages are outlined schematically in Figure 1. In stage 1, a fabricated opal template, Figure 1a, is infiltrated with a thin sacrificial buffer layer (Fig. 1b). The sacrificial layer modifies the original opal template to create a new template for patterning the desired dielectric material. Figure 1c shows the multilayer infiltrated opal template after depositing an additional dielectric film. In

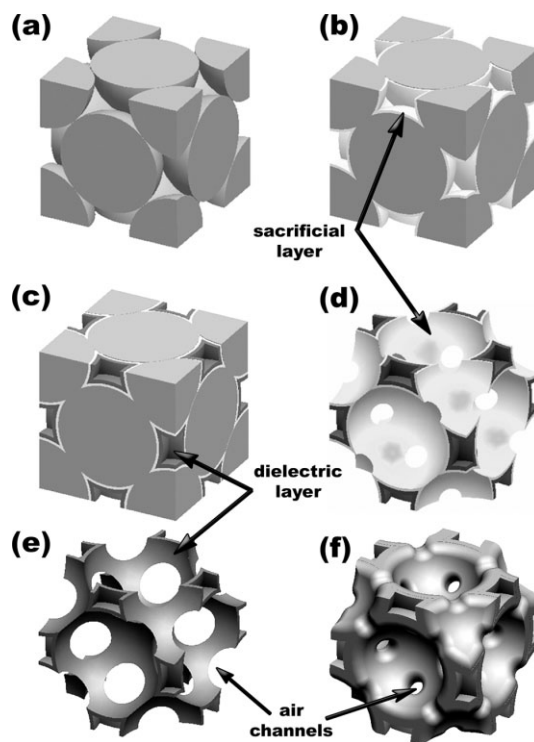


**Figure 1.** Template-patterned sacrificial-layer ALD applied to create an NCP inverse opal. The original opal template in (a) is coated with a conformal thin film, resulting in the new template shown in (b). c) A second ALD infiltration is performed in the remaining air volume. For conformal deposition techniques, maximum opal infiltration is achieved at ca. 86%, leaving small air pockets at the centers of the voids. d) Removal of the original template creates a lattice of close-packed interconnected air spheres in a multilayered dielectric matrix. e) A lattice of overlapping air spheres forms by removing the sacrificial buffer layer. Large air channels now connect the air spheres. f) Backfilling with additional dielectric forms an NCP lattice of separated air spheres, which are connected by small air tubes.

stage 2, the original opal template is first removed, creating a two-layer inverse opal (Fig. 1d). The lattice of air spheres is interconnected by holes or channels in the matrix resulting from the contact points of the silica spheres. Next, the sacrificial layer is removed producing an inverse opal, shown in Figure 1e, consisting of overlapping air spheres in a dielectric matrix. As a result, the air channels connecting the spheres are increased in size, creating large pores proportional to the degree of overlap between the spheres, which is precisely controlled by the thickness of the sacrificial layer. The precision of the layer thickness is determined by the ALD growth rate and is as low as 0.51 Å/cycle. In the third stage, the inverse opal becomes a second template and is conformally backfilled with additional dielectric material to produce an NCP inverse opal where the air spheres become separated and connected by air tubes, as shown in Figure 1f. The diameter of the air spheres and the size of the air connection tubes are now both determined by the thickness of the backfilled layer, which can be precisely selected to tune the optical properties of the film. Specifically, the Bragg and higher-order band features can be adjusted over a large spectral range.

## 2. Results and Discussion

### 2.1. NCP Inverse-Opal Fabrication

This fabrication protocol was implemented using 10  $\mu\text{m}$  thick silica opal films as the template with either a ZnS or  $\text{Al}_2\text{O}_3$  sacrificial buffer layer and a  $\text{TiO}_2$  dielectric backbone, each of which was deposited by ALD using standard precursors, as described elsewhere.<sup>[12,14,20]</sup> ALD utilizes cyclic sequential self-limiting surface reactions to grow smooth (root-mean-square (rms) roughness  $< 1$  nm), conformal thin films one layer per cycle.<sup>[21]</sup> Since ALD is a precise, “digital”, film-growth technique, sub-nanometer fine-tuning of the ratios of infiltrated material is easily accomplished. In fact, the average deposition rate of  $\text{TiO}_2$  for these experiments occurred at  $0.51 \text{ \AA}/\text{cycle}$ , leading to ultrafine control of the deposited film. Scanning electron microscope (SEM) images in Figure 2 demonstrate the main stages of fabrication. The result of the first stage is shown in Figure 2a, which is a cross section of a doubly infiltrated silica opal template after ion-milling to remove the top half of the outer layer of spheres. The air voids of the template were first infiltrated with ZnS to a thickness of 15 nm, and then infiltrated with 20 nm of amorphous  $\text{TiO}_2$  to fill the remainder of the voids. For conformal coatings within opal templates, the maximum infiltration thickness occurs at 7.75 % of the sphere diameter, which is determined by closure of the pores in the (111) surface. Thus, the maximum infiltration thickness of 35 nm for a 450 nm opal gives a ZnS/ $\text{TiO}_2$  infiltration thickness ratio of 3:4. The inset of Figure 2a shows a high-magnification image at the contact point of two spheres. The infiltrated ZnS and  $\text{TiO}_2$  films are clearly distinguished, and each shows no porosity and excellent conformality to the silica spheres, even at the ultrasharp ( $< 10$  nm) sphere contact point. No other deposition technique is capable of this level of quality and control.

Figure 2b shows the second stage, where the silica spheres and sacrificial ZnS layer have been removed, leaving only a thin backbone of  $\text{TiO}_2$ . In effect, the deposition of the sacrificial ZnS layer increased the size of the template spheres without changing the periodicity of the structure. Thus, when the spheres and the sacrificial layer were removed, a network of overlapping air spheres remained, entirely consistent with the schematic presented in Figure 1e and highlighted by the dashed-line overlay. The air spheres had a larger effective diameter than the initial starting spheres: ca. 477 nm compared to 450 nm for the silica spheres used in the original template. This measured air-sphere diameter agreed well with the expected diameter, which was increased from the silica-sphere diameter by twice the sacrificial layer thickness ( $\sim 30$  nm). Also, the ca. 211 nm average diameter of the air channels, corresponding to the necking regions, was much larger than those formed in a conventional inverse opal ( $\sim 50$  nm), where the connectivity between spheres is controlled by high-temperature sintering. Sintering is a technique that requires extremely precise temperature and time control, is incompatible with many template materials and structures, and may induce undesired material-property changes, such as changes in phase, porosity, and refractive index. Fabrication of the overlapping,

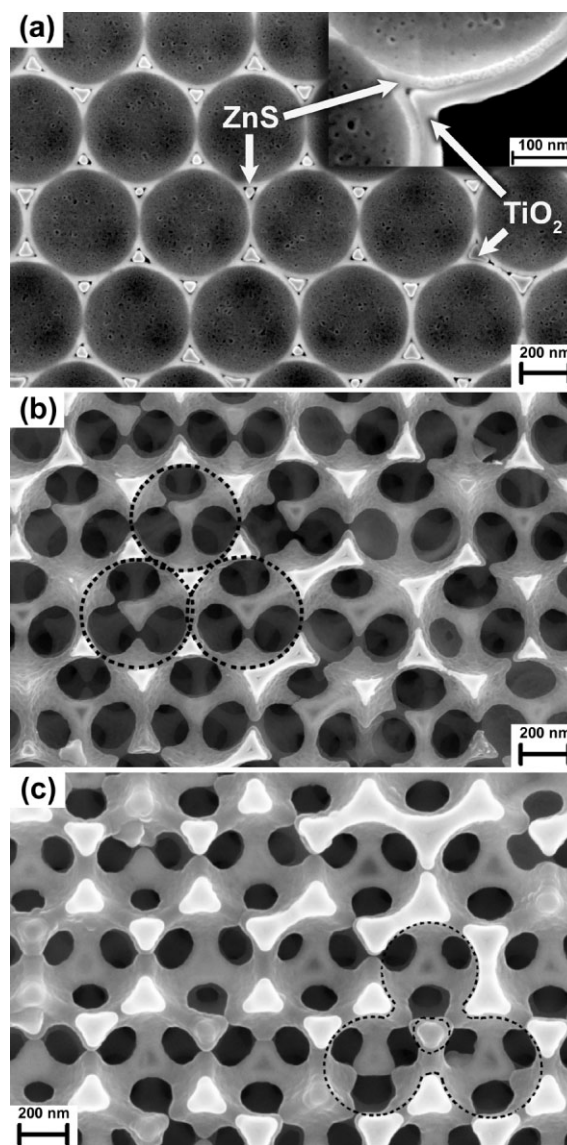


**Figure 2.** SEM images of ion-milled cross sections showing the three main stages of NCP inverse-opal fabrication. a) Stage 1: A two-layer infiltrated 450 nm  $\text{SiO}_2$  opal with a 15 nm sacrificial ZnS layer and 20 nm  $\text{TiO}_2$  infiltration. b) Stage 2: The  $\text{SiO}_2$  spheres and the ZnS layer have been removed from the sample shown in (a) leaving a lattice of overlapping air spheres in a  $\text{TiO}_2$  backbone. c) Stage 3: The sample has been backfilled with 20 nm of  $\text{TiO}_2$ , creating an NCP inverse opal.

large-pore structures shown in Figure 2b was only possible through controlled surface-limited film growth, such as that achieved by ALD, where the film shown represents an ultralow volume filling fraction of only ca. 5 %, yet is still structurally stable, reflecting the high density of the amorphous  $\text{TiO}_2$  backbone. Thus, with this new technique, ultralow-volume-fraction backbone structures were formed, which, with large-diameter air channels, allowed the structure to be re-infiltrated with a large filling-fraction of additional material.

Figure 2c shows the third fabrication stage, after the inverse-opal film was backfilled with 20 nm of additional  $\text{TiO}_2$ , producing an NCP inverse opal consisting of separated and reduced-di-

ameter air spheres connected by tubular air channels, as highlighted by the dashed-line overlay. The additional TiO<sub>2</sub> coating reduced the average air-sphere diameter from 477 to 438 nm, which is significantly smaller than the sphere diameter of the original template. The same process also reduced the air-channel diameter to 160 nm; however, this was still significantly larger than the connections in a conventional inverse opal (typically ca. 50 nm for this sphere size), thus permitting extensive backfilling that allowed for greater structural control and increased the optical tunability by over an order of magnitude from that previously reported for inverse-opal structures. We note that variation in the pore size, observed in Figures 2b and c, result from variations in the initial template and not from the fabrication process. By using improved fabrication processes for the initial template, such as isothermal vertical deposition or holographic lithography,<sup>[22,23]</sup> these variations can be greatly reduced, which translates to reduced variations in the final structure.

In addition to the finesse that the sacrificial-layer ALD technique offers in defining the NCP inverse-opal structures, it also provides a less-destructive pathway for fabricating tunable inverse opals. Figure 3 compares SEM images of samples pre-

pared by the sacrificial-layer and presintering techniques. The sacrificial-layer ALD sample in Figure 3a shows a much lower fracture density than the presintered sample shown in Figure 3b. It is also noteworthy that the sample shown in Figure 3a was fired prior to infiltration, illustrating the drastic difference between mild firing and heavy sintering. The heavy presintering required (1000 °C, 3 h) to significantly coalesce the silica spheres creates large stress fractures in the film that reduce the large-scale optical quality of the final NCP inverse-opal film. The fractures seen in the sacrificial-layer ALD sample were not formed through the ALD process, but rather were present in the initial opal template and result from the template-drying process. By utilizing alternate opal-template fabrication techniques, such as the recently reported isothermal vertical deposition,<sup>[22]</sup> the density of surface cracks can be reduced even further.

The initial fabrication steps reported here (before backfilling) produced structures similar to the Si/Ge multilayer structures fabricated by García-Santamaría et al.;<sup>[16]</sup> however, there are several significant differences. The TiO<sub>2</sub> photonic crystals fabricated here allow operation in the vis–NIR spectral region, below the range applicable to Si/Ge structures. ALD does not produce undesired growth formations that can result from Ge deposition and allows much finer control than Si and Ge CVD growth. Additionally, a major advantage of this technique is the availability of low-temperature ALD (less than 80 °C for TiO<sub>2</sub>) for applications to polymer and bioderived templates that would not survive the temperatures required for Si and Ge deposition.

## 2.2. Optical Characterization

To study the optical quality of the films, the properties of the Bragg diffraction peak were determined from specular reflectance measurements after each critical stage of fabrication: from the initial sintered opal template, after the progressive infiltrations of the opal, after the inversion and removal of the sacrificial buffer layer, and, finally, after progressive backfilling of the inverse opal. Figure 4 plots the reflectance spectra acquired at 15° to normal incidence. The spectra have been offset vertically for clarity. The reflectance spectra of the original template exhibit a peak at ca. 955 nm (FWHM = 55 nm,  $\Delta\lambda/\lambda = 5.8\%$ ; FWHM: full width at half maximum) corresponding to Bragg diffraction from the (111) planes of the opal. Upon ZnS infiltration, high-order photonic band features appeared, and the Bragg peak shifted to a longer wavelength of 1088 nm, consistent with the increase in the effective dielectric constant of the opal film. TiO<sub>2</sub> infiltration into the remaining voids produced a further shift of the photonic band features to longer wavelengths, such that the Bragg peak moved into the IR region of the electromagnetic spectrum, exhibiting a peak at 1174 nm. However, a new feature, a broad region of enhanced reflectance attributed to strong high-order photonic band features, was observed in the range 550–800 nm. Removal of the silica spheres and the ZnS sacrificial layer reduced the effective dielectric constant, resulting in a Bragg-peak shift to a shorter wavelength of 822 nm and a shift of the

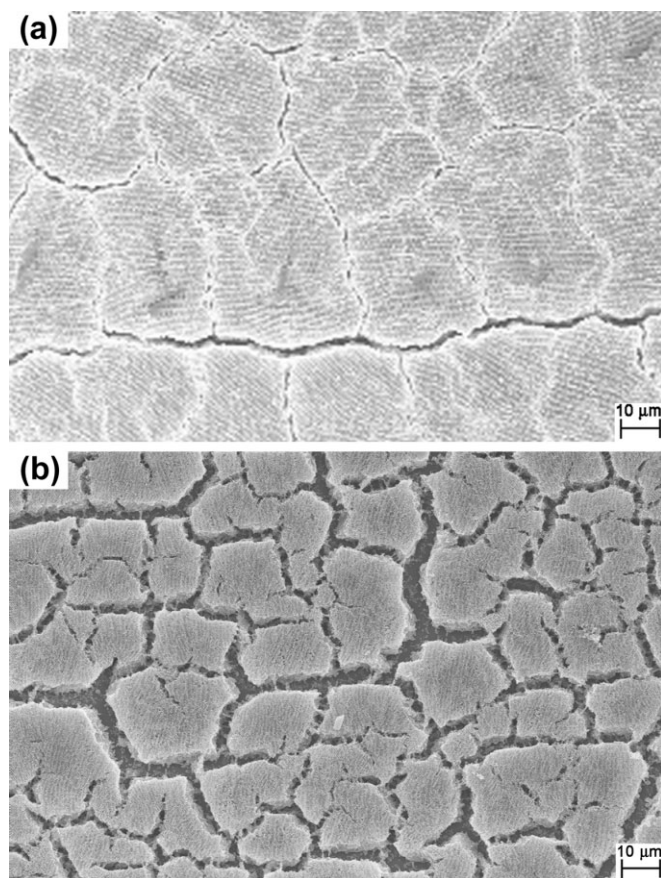


**Figure 3.** Large-area SEM images of the top surface of a sacrificial-layer NCP opal (a) and a heavily presintered NCP inverse opal (b). The sacrificial-layer NCP inverse opal shows a significantly lower density of surface cracks and smaller fractures, resulting in a much-higher-quality photonic crystal. Any defects present in the sacrificial-layer film were already present in the template.

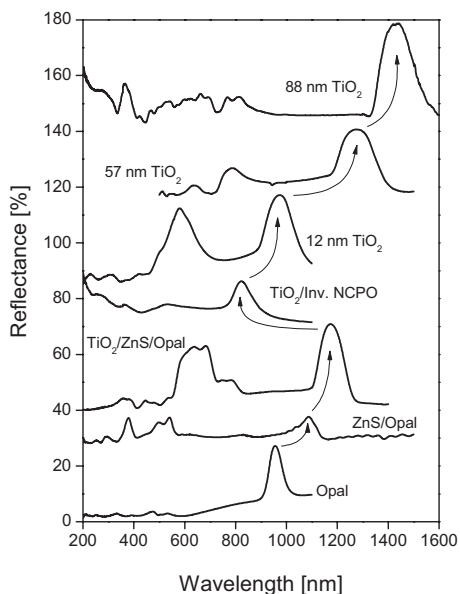


**Figure 4.** Evolution of the specular reflectance during the fabrication stages of an NCP inverse opal. The spectra have been offset vertically for clarity. The initial sintered opal exhibited a Bragg peak at ca. 955 nm. Upon infiltration with 15 nm of ZnS, the Bragg peak shifted to a wavelength of 1088 nm. A second infiltration of 20 nm of TiO<sub>2</sub> shifted the Bragg peak still further into the IR spectral region at 1174 nm; however, new strong high-order band features appeared between 550 and 800 nm. Following removal of the SiO<sub>2</sub> and ZnS by wet etching, the Bragg peak of the TiO<sub>2</sub> NCP inverse opal (NCPO) shifted back into the visible region at 820 nm. Successively backfilling the NCP inverse opal with additional TiO<sub>2</sub> increased the average refractive index and progressively shifted the Bragg peak to longer wavelengths.

high-order photonic band features into the UV region. Thus, by tuning the sacrificial-layer thickness, the Bragg peak of the resulting inverse opal shifted to a wavelength 133 nm lower than the peak of the initial template and had a TiO<sub>2</sub> filling fraction of only 5 %, significantly less than a conventional inverse opal. As shown in Figure 4, in the third stage following successive backfills of TiO<sub>2</sub>, both the wavelength and width of the Bragg peak increased. For example, when backfilled with 57 nm of TiO<sub>2</sub> the peak shifted to 1275 nm with a FWHM of 153 nm, compared to a FWHM of 88 nm at 820 nm for no backfilling.

The evolution of the optical properties was followed by analyzing the Bragg peak after each TiO<sub>2</sub> backfilling step. For an inverse opal, the wavelength of the Bragg peak ( $\lambda_{\text{Bragg}}$ ) can be approximated by

$$\lambda_{\text{Bragg}} = 2\sqrt{\frac{2}{3}}D\sqrt{1-f+n^2f} \quad (1)$$

where  $D$  is the sphere diameter. The refractive index of TiO<sub>2</sub> is both phase and wavelength dependent, ranging from 2.65 at 500 nm to 2.43 at 1450 nm for the anatase phase, and 2.45 at 500 nm to 2.25 at 1450 nm for amorphous TiO<sub>2</sub>. The step size of backfilling was initially 40 cycles, or 2 nm, and was increased to 100 cycles, or 5 nm, as the peak shifted into the IR spectral

region. Thus, gaps in the data resulted from changes in the number of ALD cycles performed between measurements. Using the wavelength-dependent refractive index of TiO<sub>2</sub> in Equation 1, Figure 5a shows plots of the Bragg-peak position

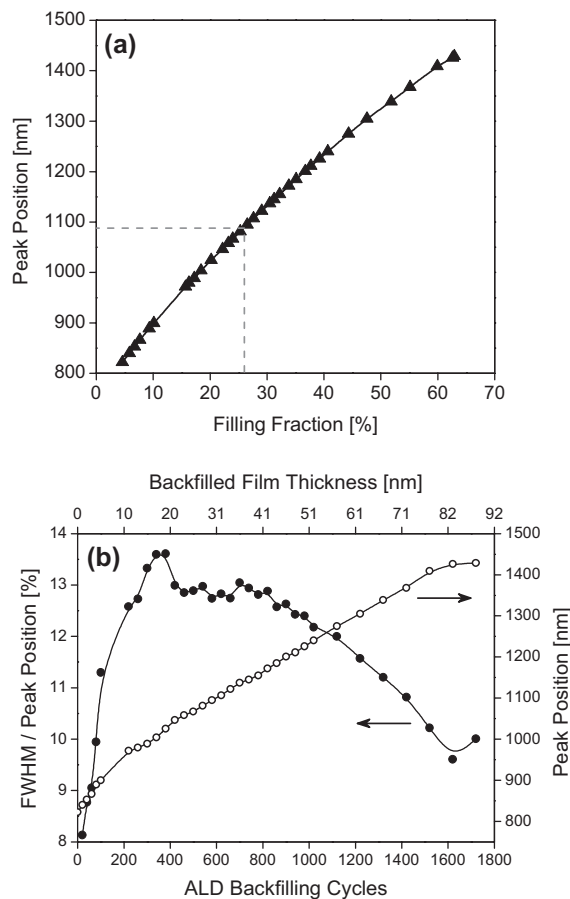


**Figure 5.** a) Bragg-peak position as a function of the TiO<sub>2</sub> filling fraction. Gaps in the data resulted from changes in the number of ALD cycles performed between measurements. The dashed line denotes the filling-fraction limit and tuning available in a conventional inverse opal. b) Measured relative width (filled-in circles, left axis) and position (open circles, right axis) of the Bragg peak versus the number of ALD cycles. The relative width reached a maximum of 13.6 % for 320 ALD cycles, which corresponds to a backfilled TiO<sub>2</sub> thickness of 20 nm.

as a function of  $f$ . Because of the large air channels created by the sacrificial layer, it was possible to vary the TiO<sub>2</sub> filling fraction from ca. 5 % to ca. 62 %, which correspondingly tuned the Bragg peak from 822 to 1429 nm. Thus, the Bragg peak was controllably tuned over 600 nm, *more than spanning the visible spectrum*, by backfilling with a total conformal coating of ca. 80 nm of TiO<sub>2</sub>. The well-behaved optical data directly confirm the finesse and precision of the whole replication process. This level of quality and control is expected to be achievable in other structures, such as 2D and 3D lithographically templated photonic crystals, since the ultrasharp features of the opal and inverse opal provide good templates for testing the robustness of the technique. In addition, the ability of ALD to deposit one

layer at a time, with a thickness of ca. 0.05 nm, allowed static tuning of the wavelength of the Bragg peak with a resolution of 0.35 nm per ALD cycle. This technique, therefore, can be applied to the tuning of both 2D and 3D structures. The deviation from linearity observed in Figure 5a is a consequence of the wavelength dependence of the refractive index of TiO<sub>2</sub>, which is especially noticeable because of the large tuning possible with these structures. The dashed line in Figure 5a shows the comparison with a conventional inverse opal, which has a maximum filling fraction of only 26 %, whereas for the NCP sample the maximum was 62 %. The precise control over such a large TiO<sub>2</sub> filling fraction and optical-tuning range was only possible using the sacrificial-layer ALD method to increase the available void volume of the inverse film and subsequently backfill the structure.

In order to assess the change of the width of the PBG during the fabrication of the NCP inverse opal, Figure 5b shows plots of the relative peak width ( $\Delta\lambda/\lambda$ ; left axis) and Bragg-peak position (right axis) of the sample as a function of ALD backfilling cycles. The corresponding film thickness is plotted along the top axis. The relative peak width increased sharply as the sample was backfilled with TiO<sub>2</sub>, reaching a maximum of 13.6 % after 380 cycles or deposition of ca. 20 nm. With further TiO<sub>2</sub> deposition, the relative width decreased to ca. 13 % and remained relatively constant until reaching 820 backfilling cycles, corresponding to 42 nm of deposition. For deposition beyond 820 cycles, a monotonic decrease in the relative width was observed to a minimum of 9.6 % after 1620 cycles (83 nm) of TiO<sub>2</sub>, at which point the air channels within the opal were closed and no further backfilling was possible. Even at this minimum, the relative peak width was higher than the original film. An additional 100 cycles produced a slight increase of the Bragg-peak width because of deposition on the outer surface of the film. The observed initial increase in the FWHM of the Bragg peak is indicative of an enhancement in the pseudo-PBG width between the second and third bands in the  $\Gamma$ -L direction of the crystal. The peak width of 13.6 % was a 67 % enhancement over the initial peak width of the inverse-opal film, representing the point just after which the NCP inverse opal transitions from having overlapping to separated air spheres. Recent calculations by Doosje et al. and Míguez et al. for silicon inverse opals showed that a maximum in the complete PBG width between the eighth and ninth bands occurs for NCP fcc structures with separated air spheres.<sup>[17,18]</sup> Even though their calculations were for the full PBG of a silicon inverse opal, it is interesting to note that the maximum of the Bragg-peak width observed here also occurred for approximately the same NCP structure that they reported. Calculations have shown that for a given dielectric constant, the NCP inverse-opal structure can produce an increase in the width of the complete (8/9) PBG.<sup>[17,18]</sup> The increase in the 8/9 gap width implies a decrease in the minimum dielectric constant required to open a full PBG. Thus, the sacrificial-layer technique may offer the possibility to controllably tune the location of the dielectric materials, enabling 3D photonic crystals with enhanced properties.

We also note that, although disorder present in the initial template will contribute to the width of the Bragg peak, the

fact that the peak width decreased after reaching a maximum value of 13.6 % indicates that the initial increase of the width was not due to the introduction of additional disorder into the structure by the processing steps, consistent with the high quality of the film shown in Figure 3a. Additionally, the reflectance actually increased during sample fabrication from 27 % for the initial opal to 40 % for the NCP inverse opal, again indicating the high quality of the process. This feature is very important not only for these structures, but also for other material and template systems. It is also interesting to note that the peak in the relative-width versus backfilling plot also corresponded to a slight decrease in the slope of the plot of Bragg-peak position the as a function of number of ALD cycles. We are currently developing a finite-difference-time-domain (FDTD) model to analyze the relative gap widths in NCP inverse structures, and our preliminary calculations indicate a peak in the gap width for certain filling fractions. Thus, the origin of these peaks will be the subject of further study.

### 2.3. Geometrical Model

Since the sacrificial-layer ALD method produces structures with reliable precision, it is possible to develop a simple geometrical model based on the critical growth parameters that can be used to predict the resulting NCP inverse opal. Figure 6 illustrates the relevant geometrical parameters that are critical for defining the final NCP structure.

Viewed along the [111] direction, Figure 6a illustrates a uniform multilayer coating of both the sacrificial and dielectric layers in the opal template. Deposition of the sacrificial layer has the effect of increasing the radius of the opal spheres without deforming the lattice or changing the lattice constant ( $a$ ),

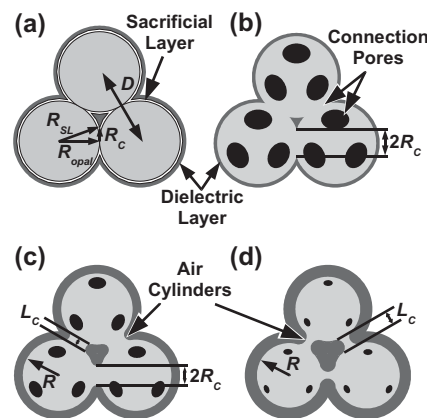


**Figure 6.** A schematic viewed along the [111] direction, illustrating the critical parameters relevant to NCP fabrication. In (a)  $R_{\text{opal}}$  and the sacrificial layer thickness,  $t_{\text{SL}}$ , define the radius of the air pores,  $R_C$ , which can be more clearly seen in the large-pore inverse opal shown in (b);  $R_{\text{SL}}$  is the radius of the overlapping dielectric spheres. In (c) backfilling with an additional dielectric layer produces an NCP inverse opal with air spheres of radius,  $R$ , separated by air cylinders of length,  $L_C$ . In (d) continued backfilling decreases, the air-sphere radius further, narrows the connecting air cylinders, and increases their length. Once the air cylinders close, further backfilling and tunability are not possible.

creating an fcc structure of overlapping dielectric spheres with radius,  $R_{SL}$ . Thus, the lattice formed with a sacrificial layer is quite different from the lattice created by sintering. The thickness of the sacrificial layer,  $t_{SL}$ , serves as a controllable parameter that can be used to adjust the degree of overlap between the spheres. Since ALD is a digital film-growth technique with thickness control below 1 nm, the sacrificial-layer thickness can be precisely chosen.

After depositing the sacrificial layer, the remaining voids in the opal template are infiltrated with a dielectric film up to the maximum filling fraction. For conformal film deposition in an unsintered opal lattice, this is equivalent to  $f=0.224$  (or ca. 86 % of the void volume) and corresponds to a maximum overlapping sphere radius of  $1.155 R_{opal}$ .<sup>[14]</sup> Thus, the maximum infiltration thickness, split between both the sacrificial and dielectric layers, is  $0.0547a$ . The dielectric material deposited in the second ALD stage creates the backbone of the inverse shell opal and also becomes the second template to pattern the backfilled material. Figure 6b shows the structure when both the opal template and sacrificial buffer layer are removed. Only the thin dielectric backbone remains, creating a lattice of overlapping air spheres, ( $R > R_{opal}$ ) connected by large air pores within a dielectric matrix. As indicated in Figure 6a, the radius,  $R_C$ , of the air pores is determined by  $R_{opal}$  and the radius of the sacrificial shell,  $R_{SL}$ , which is given by

$$R_{SL} = R_{opal} + t_{SL} \quad (2)$$

Thus, the radius,  $R_C$ , of the connecting air cylinders between the overlapping spheres is

$$R_C = \sqrt{R_{SL}^2 - R_{opal}^2} + \Delta = \sqrt{2R_{opal} \times t_{SL} + t_{SL}^2} + \Delta \quad (3)$$

where  $\Delta$  represents the minimum pore radius experimentally achievable, which depends on the surface roughness of the opal spheres.

Fabrication of the NCP structure and tunability are achieved by backfilling the inverse backbone template with additional dielectric material, as shown progressively in Figures 6c and d. Backfilling the inverse template reduces the radius of both the air spheres and the connection pores and effectively transforms the pores into air cylinders. By continued backfilling, the air-sphere radius is reduced to the point where the spheres no longer overlap ( $R < R_{opal}$ ), but become separated, as shown in Figure 6c. The radius of the separated NCP air spheres is given by

$$R = R_{SL} - t_{BF} = R_{opal} + t_{SL} - t_{BF} \quad (4)$$

where  $t_{BF}$  is the thickness of the backfilled layer. The air cylinders in Figures 6c and d now have a radius,  $R_C^{BF}$ , and length,  $L_C$ , given by:

$$R_C^{BF} = R_C - t_{BF}$$

$$L_C = 2(R_{opal} - R) = 2(t_{BF} - t_{SL}) \quad (5)$$

where  $L_C$  is only valid for  $t_{BF}$  greater than  $t_{SL}$ . The maximum thickness of the backfilled layer is limited by the connecting

pores in the inverse opal and is equal to the radius of the air cylinders in the overlapping inverse structure,  $t_{max}^{BF} = R_C$ , which increases with  $t_{SL}$  and the initial sphere diameter. Within this limit, the thickness of the backfilled dielectric layer can be chosen to tune the optical properties of the film (specifically, the position and width of the Bragg peak and the properties of the higher-order band features) over a large spectral range.

Thus, because of the smooth conformal nature of the film grown by ALD, the final structure of an NCP inverse shell opal can be approximated using a simple geometrical model. This technique allows the growth parameters necessary to achieve a desired structure to be predetermined and, in principle, sacrificial-layer ALD can be applied to a variety of other templates to create other 3D device structures. Additionally, the control provided by ALD for both the sacrificial and backfilled layers allows high precision in both fabrication and tuning of any structure.

In Figure 7, the relevant geometrical parameters are indicated for a doubly infiltrated  $SiO_2$  opal that was fabricated with a thin  $Al_2O_3$  sacrificial layer and a  $TiO_2$  backbone. As in Figure 2, the sample was ion-milled to remove the top half of the (111) plane of the spheres. As can be seen in the image, even a thin sacrificial layer increases the pore size by nearly a factor of two, greatly enhancing the air connectivity formed upon inversion.

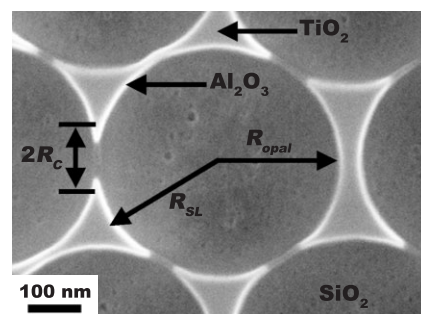


**Figure 7.** SEM image of a 450 nm silica-opal template coated with a 10 nm  $Al_2O_3$  sacrificial layer and a thicker  $TiO_2$  backbone. The geometrical parameters are illustrated on the image. As shown, the thickness of the  $Al_2O_3$  layer controls the radius of the air spheres and connecting air cylinders.

## 2.4. Dielectric Filling Fraction: Doosje Model

To quantify the degree of structural control and optical tunability possible with this technique and to compare the geometrical model to the experimental data, we have modeled the dependence of the Bragg-peak tunability on the structural parameters, specifically, the thicknesses of the sacrificial and backfilling layers. This is demonstrated in Figure 8a where the normalized frequency of the (111) Bragg peak is plotted versus the backfilling thickness for sacrificial layers of 2, 4, 6, 6.8, and 10 % of the opal-sphere radius. A sacrificial layer of 10 % is near the experimental limit since it leaves only 5.5 % for the dielectric backbone. The calculations are for NCP structures

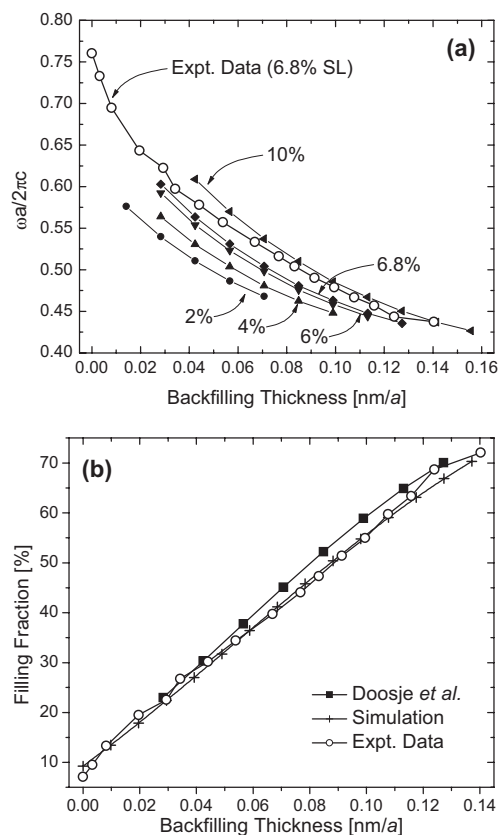


**Figure 8.** a) Calculated and experimental normalized Bragg-peak position as a function of dielectric backfilling thickness. The experimental data is for a sacrificial-layer thickness of 6.8% and the calculations are for sacrificial layer thicknesses of 2, 4, 6, 6.8, and 10% of the opal-sphere radius. These values are well below the theoretical maximum infiltration of 15.5% in order to leave volume available for the dielectric backbone. The 6.8% calculation slightly underestimates the experimental data. For the 10% sacrificial layer, an initial  $R_C$  of  $\sim 0.162a$  predicts a tunability of 80%. b) Calculated, simulated, and experimental filling fractions versus dielectric backfilling thickness. The geometrical model and the simulated structures agree closely with the data, but the simulation shows a better fit and allows the full range of filling fractions to be calculated.

( $R < R_{\text{opal}}$ ) with  $f$  related to conformal film thickness through Equation 10 of a previous publication,<sup>[17]</sup> which presents a purely geometrical model of air spheres connected by air tubes in a fully infiltrated NCP inverse opal. In terms of the sacrificial-layer model, this equation becomes

$$f = 1 - f_{\text{air}}$$

$$= 1 + \frac{80}{3} \pi (R/a)^3 - 12\pi \sqrt{2} (R/a)^2 - 32\pi \left( \frac{\sqrt{R^2 - R_C^2}}{a} \right)^3 \quad (6)$$

where  $R$  and  $R_C$  have been already defined, respectively, by Equations 4 and 5 above. Since conformal deposition results in shell-like inverse opals (less than full infiltration), the calculated filling fraction of Equation 6 was reduced by 3.6% to account for the small air pockets remaining at the centers of the opal voids. For each calculation, maximum infiltration of the

opal void volume was assumed. Thicker sacrificial layers reduced the infiltration volume available for the dielectric backbone prior to inverting the opal. Thus, with increasing sacrificial-layer thickness, the initial filling fraction of dielectric material was lower and the initial Bragg peak was observed at higher normalized frequency. However, when the structure was inverted and the sacrificial layer was removed, a larger internal air volume was created and a larger total fraction of dielectric material could be deposited, leading to a greater range of tunability. A Monte Carlo simulation was used to determine the dielectric filling fractions for increasing sacrificial-layer thicknesses. For a sacrificial-layer thickness that is 10% of the opal sphere radius, the Bragg peak is predicted to be tunable by 80%, which can comfortably span the visible spectral region (400–700 nm). Thus, by simply controlling the thickness of the sacrificial layer and the thickness of backfilled dielectric material, the optical properties of the inverse opal film can be tuned over an unprecedented range. Furthermore, as discussed above, the sub-nanometer digital growth of ALD allows the position of the band features to be precisely selected.

When compared to the experimental data (6.8% sacrificial layer), the predicted tunability of the geometrical model was very similar to that achieved by backfilling the NCP inverse opal. The calculation for a 6.8% sacrificial layer closely followed the experimental data; however, the experimental position of the Bragg peak was observed at a higher normalized frequency for a given backfilling thickness. The higher normalized frequency indicated that the dielectric filling fraction in the experimental structure was lower for a given level of backfilling than in the geometrical structure. This lower experimental filling fraction results from the smoothing effect of conformal deposition. In the geometrical model, sharp corners are present between the air cylinders and the air spheres, whereas in the fabricated structures, these sharp features were smoothed out with increasing backfill thickness. This smoothing effect can be seen by comparing Figures 2b and c.

## 2.5. Dielectric Filling Fraction: Numerical Simulation

While the geometrical model of Doosje et al. provides a convenient analytical formula for the NCP filling fraction, it does not accurately represent experimentally fabricated structures and is only valid for structures where the air-sphere diameter is smaller than the initial opal-sphere diameter. Thus, to better understand the experimental data, including when the air-sphere radius is larger than the template spheres, a model was developed to more accurately simulate the dielectric structures formed through the sacrificial-layer ALD process. In this simulation, an ideal opal template was constructed in a high-resolution grid using a  $250 \times 250 \times 250$  point matrix to represent one-eighth of the template unit cell. The conformal sacrificial layer and dielectric backbone were defined by increasing the diameter of the template spheres to create overlapping spheres with different dielectric constants. The layers were only defined in air regions of the initial template. To invert the structure, all points occupied by either the template spheres or the sacrificial

layer were set to be air by redefining the dielectric constant for those points. To conformally backfill the inverse structure, a coating algorithm was developed to emulate ALD on the surface of the dielectric backbone. The matrix was searched for dielectric/air interfaces, at which point a dielectric sphere of  $8 \times 8 \times 8$  points was inserted into the dielectric matrix. In this way, each interface point is coated with four units. This algorithm was repeated to achieve the desired backfilling thickness.

After each coating, the dielectric filling fraction was calculated by determining the ratios of the dielectric constants in the cell. The resulting filling fractions are plotted versus backfilling thickness in Figure 8b. The data from the simulated NCP inverse opal track the experimental data very well, thus providing a much more accurate filling fraction for the entire range of dielectric backfilling. The 6.8 % sacrificial-layer calculation based on the geometrical model of Doosje et al., which is plotted in Figure 8b for comparison, is only valid once the air sphere radius is less than the original opal sphere radius (i.e., only for an NCP inverse opal). Thus, the developed coating algorithm provides a method to precisely determine the filling fractions and optical properties of NCP inverse opals during the entire fabrication process. Based on the calculated filling fraction, the Bragg peak position can be easily calculated from the Bragg diffraction equation given in Equation 1, although we are currently investigating the simulated dielectric functions for calculating the full photonic band diagram for each structure using the FDTD method. Additionally, for a given sphere radius, the deposition parameters for high-index materials required to produce the largest PBGs (both high and low order) can be reliably calculated.

### 3. Conclusions

We have reported the controllable fabrication of tunable  $\text{TiO}_2$  NCP inverse-shell opals using template-patterned sacrificial-layer ALD and have developed a geometrical model to define the structural parameters that are critical to fabrication. Sacrificial-layer ALD provided a robust fabrication route with low-temperature, sub-nanometer, layer-by-layer precision, offering far greater control than techniques that involve high-temperature processing or template-etching pretreatments,<sup>[18,24]</sup> and produced fundamentally different structures. The high quality, smooth, and exact inverted replication of complex 3D geometries that was obtained for the inverse opals highlights the ability of ALD to produce uniform coatings with minimal porosity. This technique produced stable structures even within an ultrathin  $\text{TiO}_2$  backbone, where the smallest structural component was less than 20 nm wide, as shown in Figure 2. The sacrificial-layer technique is clearly superior to sintering methods in terms of film quality and the ability to control the optical properties of fabricated structures. This technique produced 3D films with greatly enhanced photonic properties, allowing the limitations of available dielectric materials to be partially overcome. Specifically, pseudo-PBG tuning of over 600 nm with a 0.35 nm precision was demonstrated, along with a 67 % increase in the width of the Bragg peak. This

level of control is also expected to be critical for tuning optical features resulting from high-order bandgaps and flat bands. With careful design of the optimized NCP inverse opal structure, this technique promises to greatly expand the potential of opal-based photonic devices, as well as other template structures.

Using the deposition parameters, dielectric filling fractions for backfilled NCP structures were calculated from a geometrical model and compared to the experimental data. To improve the extent and accuracy of the calculations, a simulation algorithm was developed to closely model the fabricated structures during the entire growth process. This simulation predicted Bragg-peak tuning of over 600 nm for a  $\text{TiO}_2$  backbone, and provided excellent agreement to the experimental data.

Also, these results demonstrate a new concept for fabricating novel nanoscale device structures with nearly independent control over structure and material composition. The template-patterned sacrificial-layer ALD procedure allows materials with different electric, magnetic, and optical properties to be patterned and combined at the nanoscale, creating new composite materials. Taking advantage of the large number of materials that can be conformally deposited by ALD,<sup>[25]</sup> either individually or in multilayer films, and combining them with the large number of templating techniques allows for the fabrication of a nearly infinite number of new optical, electronic, and magnetic device structures. Furthermore, the tunability afforded by this technique allows optimization and has widespread application to these and other devices. We have also shown that ultrasoft  $\text{TiO}_2$  films can be deposited at low temperatures (below 80 °C) to allow the combination of sacrificial-layer ALD with polymer and biologically derived structures, further increasing the scope of this concept by allowing it to utilize templates derived through any process. Thus, sacrificial-layer ALD helps to overcome the limitations imposed by any single templating technique and promises to be a powerful tool for advancing materials science to greater levels of control than currently available.

### 4. Experimental

Monodisperse silica colloids were formed using the Stöber method and dispersed in ultrapure deionized (DI) water [26]. 10  $\mu\text{m}$  thick silica opal films were next grown by forced sedimentation in a confinement cell [27]. After mildly firing the opal films in air at 800 °C for 2 h, a Microchemistry, Ltd. F120 ALD tool was used to deposit ZnS films within the opal. The ALD deposition sequence consisted of alternating 2 s pulses of  $\text{ZnCl}_2$  and  $\text{H}_2\text{S}$ , each separated by a 2 s  $\text{N}_2$  purge, while maintaining the substrate at 500 °C. Opals with sphere sizes of 450 nm were used in this study. The samples were infiltrated with 2.5, 5, 15, or 30 nm thick layers of ZnS whose thicknesses were projected from the planar growth rate of 0.78 Å/cycle. Sacrificial layers of  $\text{Al}_2\text{O}_3$  were deposited in unsintered opal films, since the sacrificial layer renders the conventional mild firing step superfluous. The  $\text{Al}_2\text{O}_3$  layers were grown at 80 °C using trimethylaluminum (TMA) and  $\text{H}_2\text{O}$  as precursors following the procedure of Groner et al. [28], with pulse times approximately doubled to allow for diffusion within the opal template.

Using a custom flow-style hot-wall ALD reactor, amorphous  $\text{TiO}_2$  (refractive index = 2.45 @ 500 nm) was grown within the opal using alternating 8 s pulses of  $\text{TiCl}_4$  and  $\text{H}_2\text{O}$ , each separated by a 20 s,

225 sccm N<sub>2</sub> purge, while maintaining the substrate at 100 °C. The vacuum level within the reactor was ~750 mTorr during pulses and 700 mTorr (1 mTorr ≈ 0.133 Pa) during purges. The precursor gases were fed into to a N<sub>2</sub> carrier gas using computer-controlled solenoid valves. Since HF acid will etch amorphous TiO<sub>2</sub>, prior to inversion the amorphous TiO<sub>2</sub> film within the infiltrated opal was converted to the crystalline anatase phase (refractive index = 2.65 @ 500 nm) by a 400 °C post-deposition heat treatment, performed in the ALD reactor under a constant N<sub>2</sub> flow rate of 225 sccm. The surface of the heat-treated opal was next ion-milled for 23 min with a 4 keV Ar<sup>+</sup> beam at 15° incidence. A 2 % HF solution was used to remove the silica spheres and Al<sub>2</sub>O<sub>3</sub> sacrificial layers, and dilute HNO<sub>3</sub> was used to remove the sacrificial ZnS layer, in each case etching three times for 30 min. The backfilled TiO<sub>2</sub> depositions were performed using the conditions described above but were not converted to the anatase phase.

All optical measurements were performed using a variable-angle specular reflectance system, which was set to 15° from the sample normal. The measurement area of the system was approximately 1 mm<sup>2</sup>. The visible and IR spectral regions were measured using biased Si and InGaAs detectors, respectively.

The finite-difference-time-domain calculations were performed using a custom FORTRAN program. Ideal opal templates were constructed in MATLAB using a high-resolution 250 × 250 × 250 point matrix to represent one eighth of the template unit cell.

Received: November 24, 2005

Final version: March 1, 2006

Published online: May 4, 2006

- [1] S. John, *Phys. Rev. Lett.* **1987**, *58*, 2486.
- [2] E. Yablonovitch, *Phys. Rev. Lett.* **1987**, *58*, 2059.
- [3] A. Yariv, P. Yeh, *Optical Waves in Crystals: Propagation and Control of Laser Radiation*, Wiley, New York **1984**.
- [4] H. M. Yates, W. R. Flavell, M. E. Pemble, N. P. Johnson, S. G. Romanov, C. M. Sotomayor-Torres, *J. Cryst. Growth* **1997**, *170*, 611.
- [5] J. E. G. J. Wijnhoven, W. L. Vos, *Science* **1998**, *281*, 802.
- [6] S. G. Romanov, R. M. De La Rue, H. M. Yates, M. E. Pemble, *J. Phys. Condens. Matter* **2000**, *12*, 339.
- [7] H. Míguez, E. Chomski, F. García-Santamaría, M. Ibisate, S. John, C. López, F. Meseguer, J. P. Mondia, G. A. Ozin, O. Toader, H. M. van Driel, *Adv. Mater.* **2001**, *13*, 1634.
- [8] K. Busch, S. John, *Phys. Rev. E* **1998**, *58*, 3896.
- [9] A. Blanco, E. Chomski, S. Grachtchak, M. Ibisate, S. John, S. W. Leonard, C. López, F. Meseguer, H. Míguez, J. P. Mondia, G. A. Ozin, O. Toader, H. M. van Driel, *Nature* **2000**, *405*, 437.
- [10] E. Palacios-Lidón, A. Blanco, M. Ibisate, F. Meseguer, C. López, J. Sánchez-Dehesa, *Appl. Phys. Lett.* **2002**, *81*, 4925.
- [11] B. H. Juárez, M. Ibisate, J. M. Palacios, C. López, *Adv. Mater.* **2003**, *15*, 319.
- [12] J. S. King, C. W. Neff, C. J. Summers, W. Park, S. Blomquist, E. Forsythe, D. Morton, *Appl. Phys. Lett.* **2003**, *83*, 2566.
- [13] A. Rügge, J. S. Becker, R. G. Gordon, S. H. Tolbert, *Nano Lett.* **2003**, *3*, 1293.
- [14] J. S. King, E. Graugnard, C. J. Summers, *Adv. Mater.* **2005**, *17*, 1010.
- [15] A. Rügge, J.-S. Park, R. G. Gordon, S. H. Tolbert, *J. Phys. Chem. B* **2005**, *109*, 3764.
- [16] F. García-Santamaría, M. Ibisate, I. Rodríguez, F. Meseguer, C. López, *Adv. Mater.* **2003**, *15*, 788.
- [17] M. Doosje, B. J. Hoenders, J. Knoester, *J. Opt. Soc. Am. B* **2000**, *17*, 600.
- [18] H. Míguez, N. Tétreault, S. M. Yang, V. Kitaev, G. A. Ozin, *Adv. Mater.* **2003**, *15*, 597.
- [19] J. S. King, D. P. Gaillot, E. Graugnard, C. J. Summers, *Adv. Mater.*, **2006**, *18*, 1063.
- [20] A. W. Ott, J. W. Klaus, J. M. Johnson, S. M. George, *Thin Solid Films* **1996**, *292*, 135.
- [21] M. Leskelä, M. Ritala, *Thin Solid Films* **2002**, *409*, 138.
- [22] S. Wong, V. Kitaev, G. A. Ozin, *J. Am. Chem. Soc.* **2003**, *125*, 15 589.
- [23] J. S. King, E. Graugnard, O. M. Roche, D. N. Sharp, J. Scrimgeour, R. G. Denning, A. J. Turberfield, C. J. Summers, *Adv. Mater.*, in press.
- [24] R. Fenollosa, F. Meseguer, *Adv. Mater.* **2003**, *15*, 1282.
- [25] M. Ritala, A. Leskelä, in *Handbook of Thin Film Materials* (Ed: H. S. Nalwa), Vol. 1, Academic Press, San Diego, CA **2001**, Ch. 2.
- [26] W. Stöber, A. Fink, E. Bohn, *J. Colloid Interface Sci.* **1968**, *26*, 62.
- [27] S. H. Park, D. Qin, Y. Xia, *Adv. Mater.* **1998**, *10*, 1028.
- [28] M. D. Groner, F. H. Fabreguette, J. W. Elam, S. M. George, *Chem. Mater.* **2004**, *16*, 639.